PHYSICAL REVIEW E **75**, 056313 (2007)

Effect of a vertically flowing water jet underneath a granular bed

F. Zoueshtiagh* and A. Merlen
Laboratoire de Mécanique de Lille UMR CNRS 8107, Bd Paul Langevin, 59655 Villeneuve d'Ascq, France

(Received 9 February 2006; revised manuscript received 5 September 2006; published 29 May 2007)

The response of a granular bed to a punctual, vertically flowing water jet underneath it is studied experimentally, theoretically, and numerically. Experiments show that three regimes depending on the flow rate Q appear to outline the bed's behavior. For sufficiently small Q, the bed remains motionless and acts as a rigid porous medium [regime (i)]. It then becomes deformed when Q is sufficiently increased [regime (ii)]. Finally, the bed "explodes" and a locally fluidized bed limited to a domain above the water jet is observed as Q is increased further [regime (iii)]. This fluidization creates a "chimney" in the bed, roughly cylindrical in shape, inside which the grains are in motion. The flow motion in regime (i) is theoretically modeled as a Darcy flow inside an unbounded granular bed while a numerical model accounting for the boundaries is performed. Results from the theory and computations are compared to experimental data and the effects of the boundaries, the bed's thickness, and the size of the jet on the flow motion inside the bed are underlined. The onset for fluidization [regime (iii)] is explained by assuming a stick-slip behavior of the chimney. Despite the simplistic model, the comparison with experimental data show very good agreement for bony sand granules and relatively good agreement for spherical glass beads.

DOI: 10.1103/PhysRevE.75.056313 PACS number(s): 47.56.+r, 47.55.Kf

I. INTRODUCTION

Fluidized beds are observed when a fluid is pumped upwards from the bottom of a granular bed. They have been studied for decades, as they are relevant to various industrial, coastal and geophysical applications. Below, an assortment of studies associated with these respective applications and of interest to our investigation are briefly presented. Thereafter, some characteristics of fluidized beds are described. Finally, the goal of the present study is presented.

Industries commonly make use of fluidized beds in the transportation of particulate solids (pneumatic transport) or as devices for mixing, heat and mass transfer, and as chemical reactors (see, e.g., [1–5]). For instance, in the case of a fluidized-granular bed over a tapered surface, extensive mixing can be achieved leading to dozens of applications such as the biological treatment of wastewater, incineration of waste materials and coating nuclear fuel particles, etc. [1–5]. Consequently, numerous industry-related studies focus on mixing systems which usually consist of an upward-fluid jet located underneath a granular bed lying on a conical or tapered surface (see, e.g., [1,3,4,6–8]).

In coastal engineering applications, analytical and laboratory research are closely associated with designs of fluidizer systems for the maintenance of navigable waterways and in sand bypassing at tidal inlets and harbor mouths (see, e.g., [9–12]). They usually make reference to the effect of punctual and regularly placed flow exits from small holes in a buried source pipe with the liquid flowing horizontally. In such configurations the sand bed is often considered by the researchers as an unbounded domain [9–12].

Concerning geophysical applications, studies usually focus on the role of subsurface flow in the soil-water erosion process, known as seepage erosion (see e.g. [13–15]). In Refs. [13,15], the authors investigated the main modes of sediment transport when a sand pile is fed with water from beneath. While Owoputi *et al.* [14] showed that soil erodibility could be affected by both the soil characteristics and the flow condition in the soil, Schorghofer *et al.* [15] carried out field and laboratory experiments on the sediment mobilization. They described the seepage erosion as a consequence of three modes of sediments mobilization: channelization, slumping and fluidization. Their experiments were followed by those of Lobkovsky *et al.* [13] who studied the threshold phenomena associated with the onset of erosion. In their setup which consisted of a rectangular box filled with glass beads shaped into a trapezoidal wedge, the water horizontally entered the sand pile underneath through a section as wide as the width of the pile. In their paper, they reported a state for which the water could emerge on the pile surface just above the water inlet without observing slumping or fluidization of the sand pile. Following their description, this state appears to correspond to a confined fluidization above the inlet while the overall shape of the pile is kept unchanged (mainly nonfluidized). As will be seen later, the present paper will focus on a similar state where a confined fluidization of a bed is obtained thanks to a punctual and vertical water jet.

Fluidized beds are subject to various behavior with increasing upward-fluid velocity. Their behaviors are classified in four main regimes: (a) Homogeneous, (b) voidage-wave instability, (c) bubbling, and (d) slugging (reviews can be found in Refs. [16–19]). Experimental studies of these regimes are usually conducted in vertical tubes where the bed to particle diameter ratio R is often of the order of 10. Depending on R values the bed can exhibit jamming or arching effects (small R), one-dimensional voidage-wave instability ($10 \lesssim R \lesssim 25$) or two-dimensional wave instability ($25 \lesssim R$) [20].

Bed responses could also depend on the nature of the flowing fluid. While liquid-fluidized beds can, for instance, exhibit 1D or 2D voidage-wave instabilities [regime (b)],

---

*Email address: Farzam.Zoueshtiagh@univ-lille1.fr gas-fluidized beds are very unstable and rapidly reach the bubbling regime. The characteristics of regime (c) in gas-fluidized beds might also vary with the particle size. For instance, experiments of Jung *et al.* [21] on nano-size particles showed that although small bubbles could form at the bottom of the bed and grow, coalesce and then burst at the top of the bed, large bubbles could not be observed.

The reported studies on the above applications with respective geometries and configurations are impressive in terms of numbers. However, it appears that the effect of a punctual fluid source underneath or inside an infinite granular bed has, surprisingly, attracted less attention. To our knowledge, besides the papers associated with coastal engineering [9–12], the few reported works are those of Refs. [22–25]. In Refs. [23,24] the authors investigated the dynamics of rising gas through an immersed layer of granular bed, while in Ref. [22] the granular temperature was studied in a pseudo 2D set-up where the bed was uniformly gas-fluidized through a porous plate but with an additional gas flow through a central nozzle. A numerical study of the latter configuration was reported in Ref. [26].

Nevertheless, a punctual-fluid source configuration may have important geophysical and fundamental interest. For instance, water-fluidized granular beds commonly observed on sand beaches or on the border of rivers, usually result from the presence of a "punctual" water source underneath a sandy bed. Figure 1 displays two photographs of such beds developing on the beaches of Georgiopoli in the Creta island. The photographs show sand patterns developing at the sand-water interface as a result of water flowing vertically from beneath. Regarding the fundamental aspect of such a system, the fluidization occurs in an environment where it has "control" over its size, i.e., its boundary. Indeed, with the bed made of cohesionless grains, the fluidized section of the bed is surrounded by friable walls which allow it "an adjustable size."

Laboratory experiments were carried out to investigate the effect of a punctual water jet underneath a granular bed. The experimental setup is described in Sec. II. Section III is devoted to the description of the phenomenon. In Sec. IV a simple theoretical model as well as a numerical model is developed. Their results are compared to experimental data and a discussion follows. Finally the findings are summarized in Sec. V.

II. EXPERIMENTAL SETUP

The experimental setup is illustrated in Fig. 2. It consists of a Plexiglas cylindrical tank of 24 cm in diameter. The bottom of the tank is made of a disk which can slide along the axis of the cylinder allowing a variation in volume of the cylinder by changing the height H from 0 to 17 cm (Fig. 2). The disk contains a central hole on which "subcylinders" with specific internal diameters can be attached. This design enables the study of the influence of water-source size by using three subcylinders of internal diameters, d_i, of 3, 15, and 35 mm. Above each subcylinder a grid of 210 μm is placed to avoid grains falling into the water-source section. Sand granules and glass beads were used in the experiments. These were previously sieved to a range of 250–450 μm and 800–1200 μm, respectively. The density of both granules is $\rho_G \approx 2.65$ g cm^{-3}. In brief, the experiments are carried out as follows. First the tank is filled to a height S with granules.

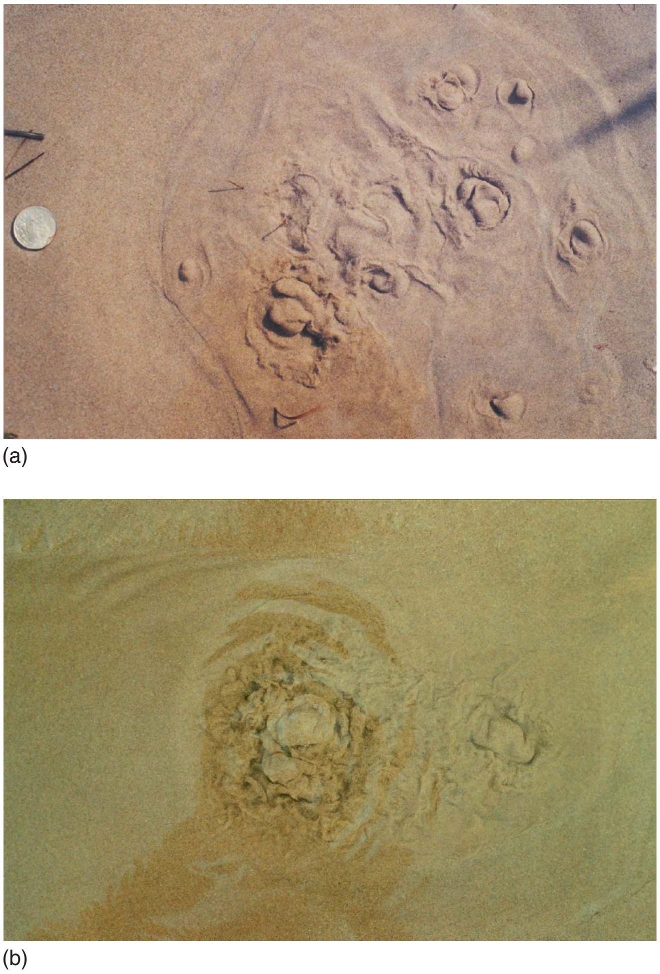

FIG. 1. (Color online) The photographs show examples of locally fluidized beds with the granular bed surface located around 4–5 cm below the air-water surface. The patterns seen on these photographs arise from the fluidized bed formed as a result of a water source flowing vertically from beneath the bed. In the present examples the patterns do not interfere with the air-water surface. The pictures width portray approximately 40 cm.

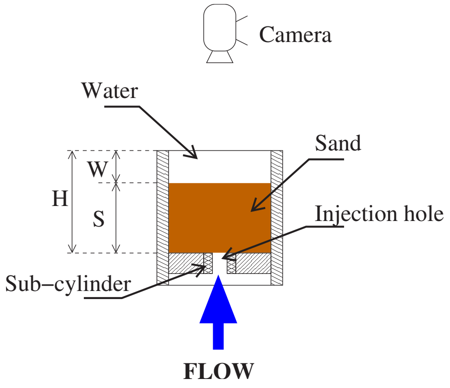

FIG. 2. (Color online) Sketch of the experimental setup.

Water is then injected vertically through the subcylinder's hole located at the bottom of the tank. The flow rate is measured with a flowmeter placed before the injection section. Once the water has fully filled the tank and reached the top of the latter, it begins to pour outside from the periphery. This allows a constant volume of water in the tank. All experiments are carried out under this state of "constant liquid volume."

In the preparatory phase for the experiment, the bed was fluidized and then slowly defluidized. According to Ref. [27], a slow defluidization leads to a constant packing fraction of 0.590 ± 0.004 regardless of the grain size. Similar behavior was then assumed in the present experiment where a constant packing fraction for the bed (at least for the fluidized area) was supposed for different height S tested.

The motion of the granular bed is captured with a CCD video camera. The camera is usually positioned above the setup as indicated in Fig. 2. However, in some cases, the camera was replaced by a mirror set horizontally at 45° angle. In this configuration, the camera is placed horizontally on the optical path of the mirror setup. This alternative setup enables both top and lateral views of the granular motion in one capture.

Flow visualization of the fluid motion at the bed surface was made using specific buoyancy neutral dye. The latter was obtained by using mixture of salt, dyed water and ethanol. In brief, the specific dye was injected very slowly with a syringe into the tank's water while at rest. The motion of the dye was then observed. If the movement of the dye was upward, salt was then added to the mixture. In the opposite case pure ethanol (of a density of 789 $\mathrm{kg/m^3}$) was added to it. This process was performed several times until almost no movement of the dye was observed. The dye was then considered as buoyancy neutral.

III. EXPERIMENTS

In this section the behavior of the granular bed is described as the flow rate Q is increased gradually. The experiments show that the bed can exhibit up to three different regimes as Q is increased. Below, these three regimes are described individually.

A. Regime (i): Motionless bed

For low flow rates, the bed remains motionless where neither deformation nor granular motion is observed. In this configuration the bed seems to act as a rigid porous medium.

B. Regime (ii): Deformation of the bed

In the second regime, a local deformation could be observed at the bed's surface for a large enough flow rate. This bump shape deformation occurred at the center of the tank just above the injection. This deformation appeared to depend slightly on the type of granules, as it was less noticeable for experiments carried out with glass beads. In all cases, this regime was a transient situation from the porous regime to fluidization.

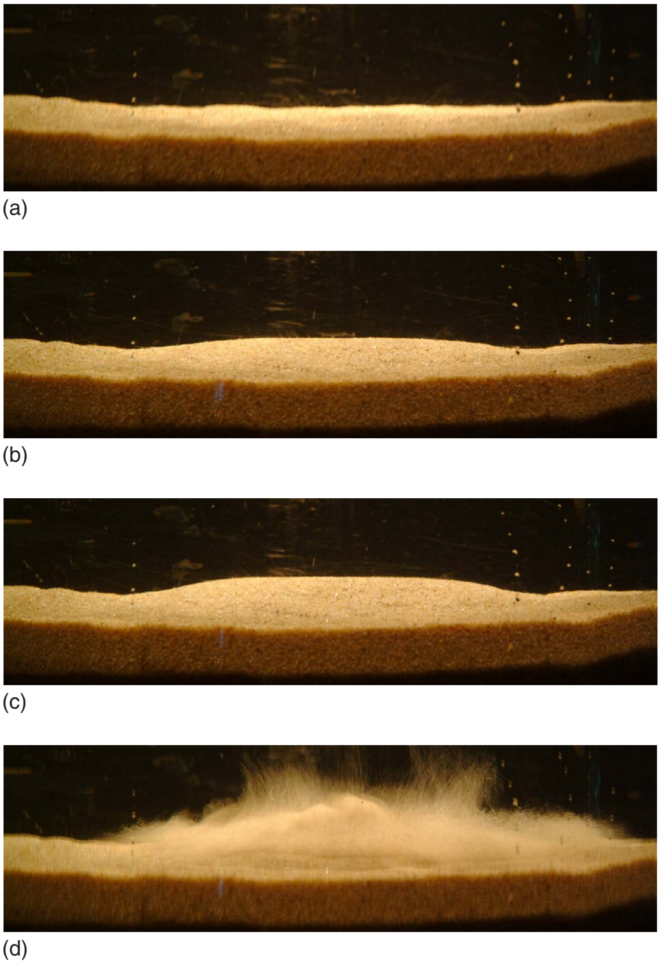

FIG. 3. (Color online) The inflation of the granular bed by the water flow. The experimental parameters are $W=7$ cm, $S=10$ cm, and $Q=80\,\mathrm{l/h}$. The above pictures are taken at (a) $t=0$ s, (b) $t=1$ s, (c) $t=2$ s, and (d) $t=3$ s. The pictures show approximately 22 cm of cell's diameter.

C. Regime (iii): Local fluidization of the bed

1. Experimental observations

In regime (iii), a fluidized area positioned over the injection hole and similar to a cylindrical and vertical chimney, is observed for Q values higher than those of regime (ii). In this regime the grains are in motion within the chimney while in the nonfluidized part of the bed they are at rest and act like a solid skeleton. The fluidization is usually preceded by a kind of "explosion" of the bed surface. Figure 3 shows a typical sequence of images taken during this bed explosion. The motion of the grains is brought to a halt when Q is decreased to values lower than those at which the fluidization occurred. We refer to these as flow rate thresholds Q_f and Q_d for fluidization and defluidization of the bed with increasing and decreasing Q, respectively.

The explosion induces the formation of a bowl-shape cavity (crater). Figure 4(a) shows a cross section view of a typical cavity formed at the onset. In this figure the flow was halted for visualization. The brightened area corresponds to a light sheet we projected along the diameter of the crater to

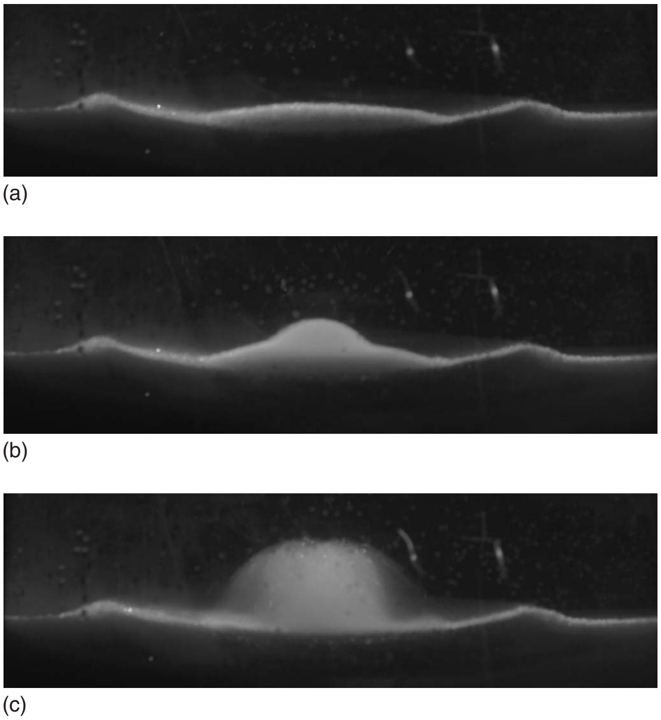

FIG. 4. A typical shape of (a) cavity formed after bed explosion, (b) a small dome composed of moving grains within the previously formed cavity, and (c) a larger dome. The pictures portray the entire diameter of the cell, i.e., 24 cm.

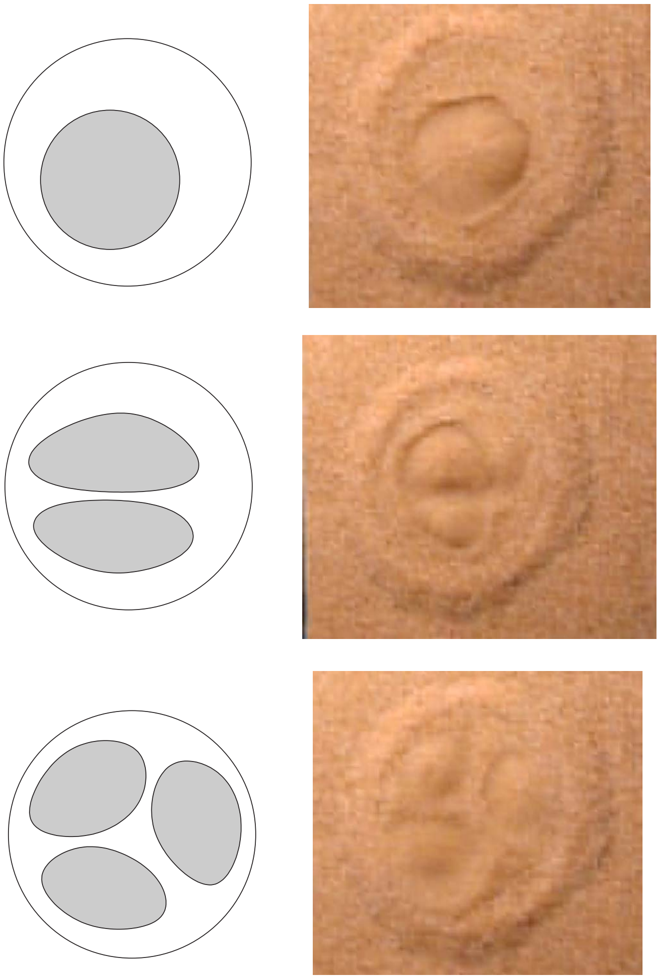

FIG. 5. (Color online) Example of patterns formed at the sand-fluid interface. The three pictures are taken at different moments during a run with $Q \approx 29$ l/h, $H=5$ cm, and $W=1$ cm. The size of the crater in these pictures is about 4 cm in diameter.

show up the shape of the cavity. The size of the cavity is usually larger than that of the fluidized area above which a dome of roughly identical size is present [see Figs. 4(b) and 4(c)]. In fact the dome is nothing else but an exhibition of the moving grains. The latter can also be animated with a fluctuating movement within the crater. The amplitude of the movement depends on the flow rate. Moreover, for large Q values, this motion exhibited a certain periodicity. The study of this oscillating motion is out of the scope of the present paper which will mainly focus on the fluidization process. However, it should be noted that an increase in Q usually induced an intensification in the motion of the dome. Large Q values could also influence the size of the dome by making it larger, which could itself increase the size of the crater.

Observations on the dome suggest that some of the granules flow to top of the dome where their vertical velocity reaches zero value. Then they start to fall toward the periphery. The number of domes observed in the experiments could vary during a run. For instance, in Fig. 5 where top view photographs of the bed are illustrated, one can see from one to three domes during the same run. In this figure a sketch drawn next to each photograph outlines the arrangement of the domes. These double or triple domes were usually unstable (typically observed during less than ≈ 1 s) and were observed for small Q and S values. Although the presence of multiple domes could appear to result from a bubbling fluidization (see, e.g., [18,28,29]), we did not have appropriate techniques to experimentally check their origin.

In all cases the size of the fluidized area remained unchanged during a run. Moreover, the concentration of moving grains in the fluidized area appeared to remain constant even after runs lasting a few hours. This suggests a recirculating motion of the grains within the chimney.

2. Results

Figures 6(a) and 6(b) show, for $d_i = 15$ mm, the fluidization and defluidization thresholds for different height S for sand and glass beads, respectively. The circle marks correspond to data obtained by gradually decreasing Q (defluidization: Q_d) while the hexagonal marks are those of increasing Q (fluidization: Q_f). Both data show linear behavior between S and Q although those of fluidization present some uncertainties. The figure indicates that a hysteresis takes place for S values larger than approximately 2.

The influence of the jet size on the flow rate onset for fluidization and defluidization is studied by using subcylinders of different internal diameters. Table I shows the measured flow rates Q_f and Q_d for different subcylinders using sand granules.

The shape of the chimney is determined using specially made vernier calipers. The latter consists of two parallel

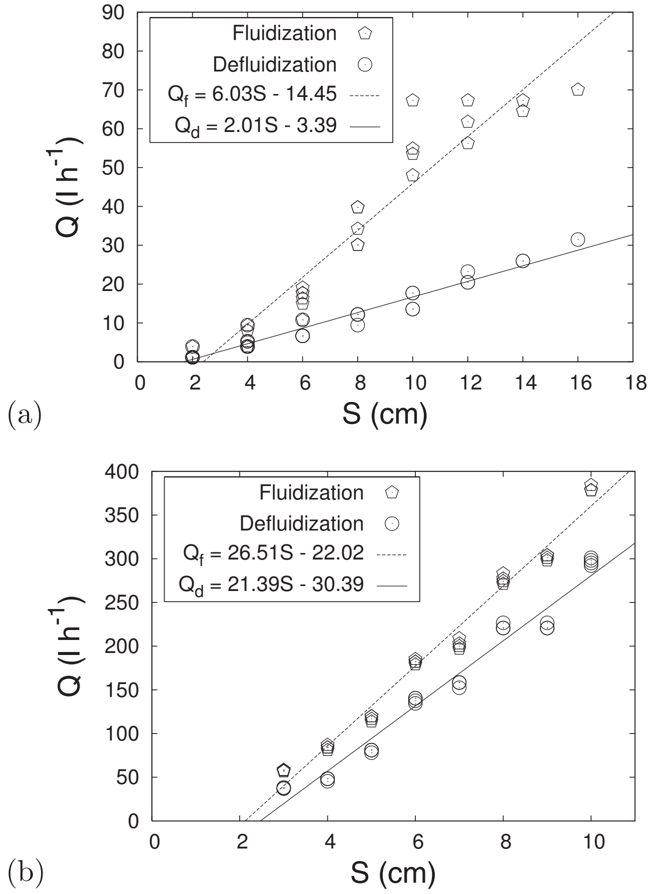

FIG. 6. Fluidization-defluidization onset recorded for different height S. The plots show data obtained with (a) sand granules and (b) glass beads. $d_i = 15$ mm.

sticks of about 1 mm in diameter with each of them attached perpendicularly to two plexiglas plates. The two plates can slide against each other in just one direction. This enables a change in the distance between the two parallel sticks. This distance can be read directly from a ruler glued onto one of the plates. The accuracy of the readings is estimated to be about ±1 mm which is comparable to the size of the sticks. In order to measure the chimney's diameter this vernier calipers is carefully dipped into the chimney until the desired depth of measure is reached (the latter can be read thanks to graduation marks made on one of the sticks). From this position, the two sticks are moved away from each other by the operator until a resistance is felt. From there, the vertical position as well as the distance between the two sticks are recorded.

TABLE I. Q_f and Q_d values recorded for different subcylinders using sand granules ($S = 16$ cm, $W = 1$ cm).

Subcylinder internal diameter d_i (mm)	Q_f (l/h)	Q_d (l/h)
3	70.05	31.48
15	70.05	31.48
35	81.06	31.48

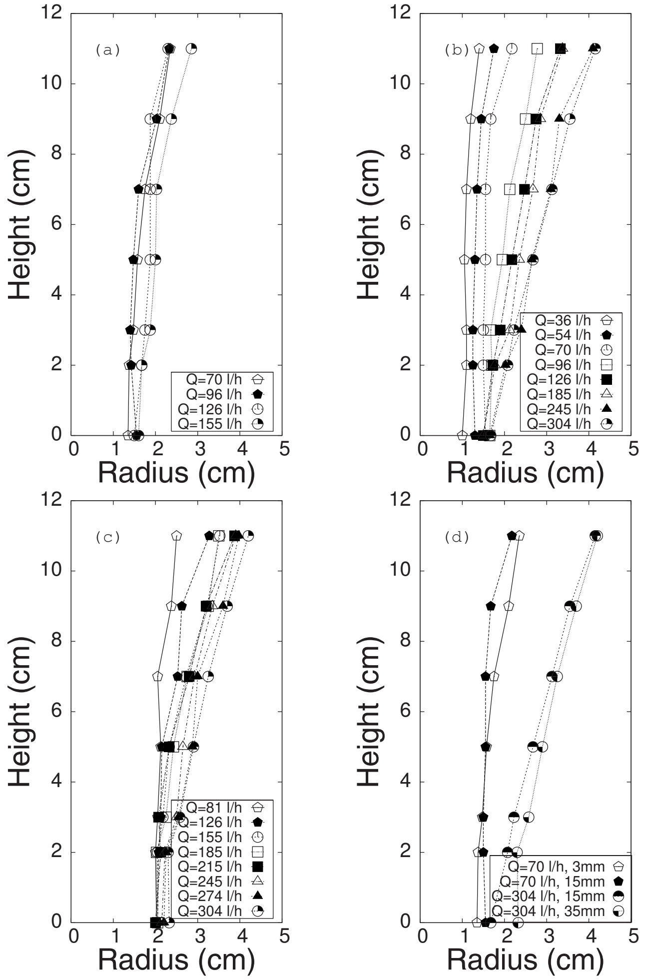

FIG. 7. The size of the chimney in a bed of sand granules of thickness $S = 12$ cm. The plots show the radius of the chimney at different flow rates for injection hole of sizes of (a) 3 mm, (b) 15 mm, and (c) 35 mm. Figure (d) compares chimney profiles obtained with different d_i but at equivalent flow rates.

Figures 7(a)–7(c) show the size (and shape) of the chimney at different flow rates for experiments carried out with sand granules. Each plot provides the profile of the chimney for a particular jet size d_i. The profiles are nearly cylindrical for low flow rates, while for large Q values they become roughly conical. The size of the chimney at the bottom of the tank appears to remain approximately constant even for large variations of Q. Figure 7(d) compares profiles obtained at a fixed flow rate but with different subcylinders (i.e., different d_i). The profiles are almost identical in size and shape despite a change in the injection diameter d_i. This might appear obvious as in Table I, the onset values of Q for bed fluidization, Q_f, or bed defluidization, Q_d, were observed to remain unchanged by a variation in d_i.

IV. ANALYSIS AND DISCUSSIONS

As was seen in the previous section there are three distinct regimes. Below the analysis is first carried out for the regimes (i) and (iii). The regime (ii) will be shortly discussed

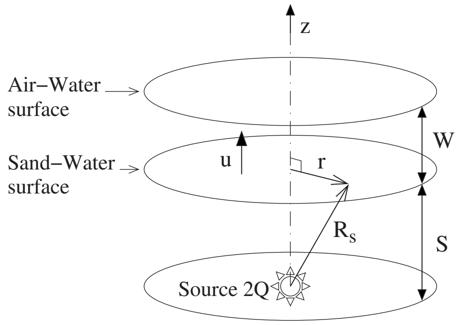

FIG. 8. Coordinates and notations.

at the end of the present section as it will be shown that it corresponds to a transitional state between regimes (i) and (iii).

A. Regime (i)

In order to verify that the bed behaves as a porous medium, it is possible to use a simple theoretical model and compare its predictions with experiments. In this regime, the flow rates have small values which yield to slow fluid motion in the water layer and at the horizontal free-surface interface air-water. Therefore, it is reasonable to assume that the flow inside the bed obeys the Darcy law and the pressure at the interface bed-water is almost constant. Hence the incompressible filtration velocity can be described by $\vec{U}=-K_D\nabla\hat{p}$ where K_D is the permeability of the bed considered constant over the thickness S and $\hat{p}=p+\rho g z$ is the driving pressure with ρ and g representing the water density and the gravitational acceleration, respectively. In the present model the origin $z=0$ is taken at the free air-water surface. Pressure $\hat{p}$ is the solution of the Laplace's equation with "almost" Dirichlet conditions $\hat{p}\simeq 0$ at the bed-water interface and an extended source at the bottom. By considering the water jet as an isolated water source underneath an infinite layer of sand, one can model the problem, in a first approximation, as analogous to the upper half part of a point source inside an infinite medium. Such a model leads to the solution $\hat{p}=Q/2\pi K_D R_s$ where R_s is the distance to the source in spherical coordinates. This solution should hold as long as the condition $d_i/S \ll 1$, or at least in the domain $d_i/R_s \ll 1$, is verified. This condition derives from the fact of representing the water jet of size d_i in our confined experiment by a punctual water source. In order to check validity of the point source model for the present experiments, numerical simulations taking into account the size of the jet as well as the confinement of the granular bed are performed. The numerical simulations are carried out as follows. Using the notations indicated in Figs. 2 and 8, the geometry of the present experiments is considered as an axisymmetric box, where Laplace's equation is solved with Dirichlet conditions $\hat{p}\simeq 0$ at the top, Neumann conditions $u_r=-K_D\partial\hat{p}/\partial r=0$ on the axis and on the lateral wall, Neumann conditions $u=-K_D\partial\hat{p}/\partial z=4Q/\pi d_i^2$ for $0\leqslant r\leqslant d_i/2$ and $u=-K_D\partial\hat{p}/\partial z=0$ for $d_i/2<r<R_e$ where R_e is the external radius of the box. This kind of formulation often used in literature [13] allows the resolution of the problem for the flow velocity without explicit value of K_D since $\Phi=\hat{p}K_D$ behaves as a velocity potential equal to zero at the top of the computational domain. Laplace's equation is written in a discrete form by a finite difference method

$$2\left(\frac{1}{\Delta r^2}+\frac{1}{\Delta z^2}\right)\Phi_{i,j}=\frac{1}{\Delta r^2}\left[\left(1+\frac{1}{2i}\right)\Phi_{i+1,j}+\left(1-\frac{1}{2i}\right)\Phi_{i-1,j}\right]+\frac{1}{\Delta z^2}(\Phi_{i,j+1}+\Phi_{i,j-1})$$

and solved on a 200×100 grid by an over-relaxation technique.

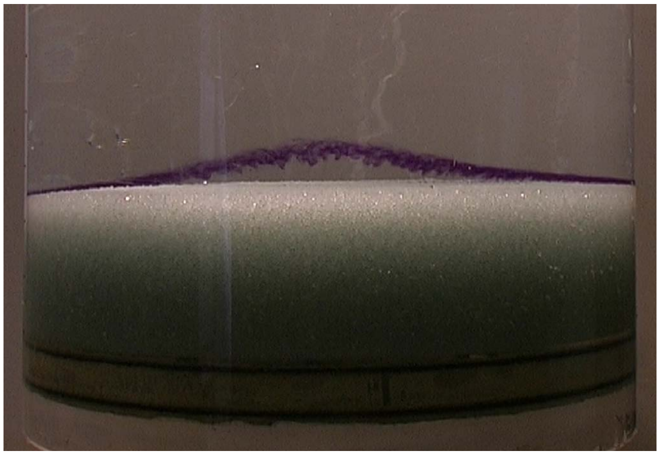

FIG. 9. (Color online) An example of images taken before fluidization of the granular bed (glass beads) while the dye is moving upwards. The dye was laid down on the surface of the bed along the diameter of the tank prior to the experiment.

Regarding the point source theoretical model, the velocity U at the bed surface at a distance $R_s=(r^2+S^2)^{1/2}$ from the source (Fig. 8) is expressed as $U=2Q/2\pi(r^2+S^2)$. The vertical velocity at the bed's surface is obtained by simple geometric considerations $u=US/R_s$ which yields:

$$\frac{u}{u_{\max}}=\left(1+\frac{r^2}{S^2}\right)^{-3/2} \tag{1}$$

with $u_{\max}=Q/2\pi S^2$. Note that the source model corresponds to an infinite domain ($R_e\rightarrow\infty$) and in order to be able to compare experimental data to theory a source emitting the same fluid mass as in the experiments in the limited region $0<r<R_e$ is needed. This is achieved by replacing the flow rate Q in the model with $(1-Z_m/\sqrt{1+Z_m^2})^{-1}Q$ where $Z_m=S/R_e$. The rescaling factor corresponds exactly to the ratio between the flow in the limited area $0<r<R_e$ and the flow in the infinite domain.

Experimentally, the profile of the vertical velocity u at the bed-water interface was visualized indirectly with buoyancy neutral dye. The latter was carefully and very slowly injected onto the bed surface diagonally across the tank while the water was at rest. The flow was then streamed in and the motion of the dye filmed with a video camera at the rate of 25 images per second. An example of a picture taken with the camera is shown in Fig. 9. The position of the dye is then

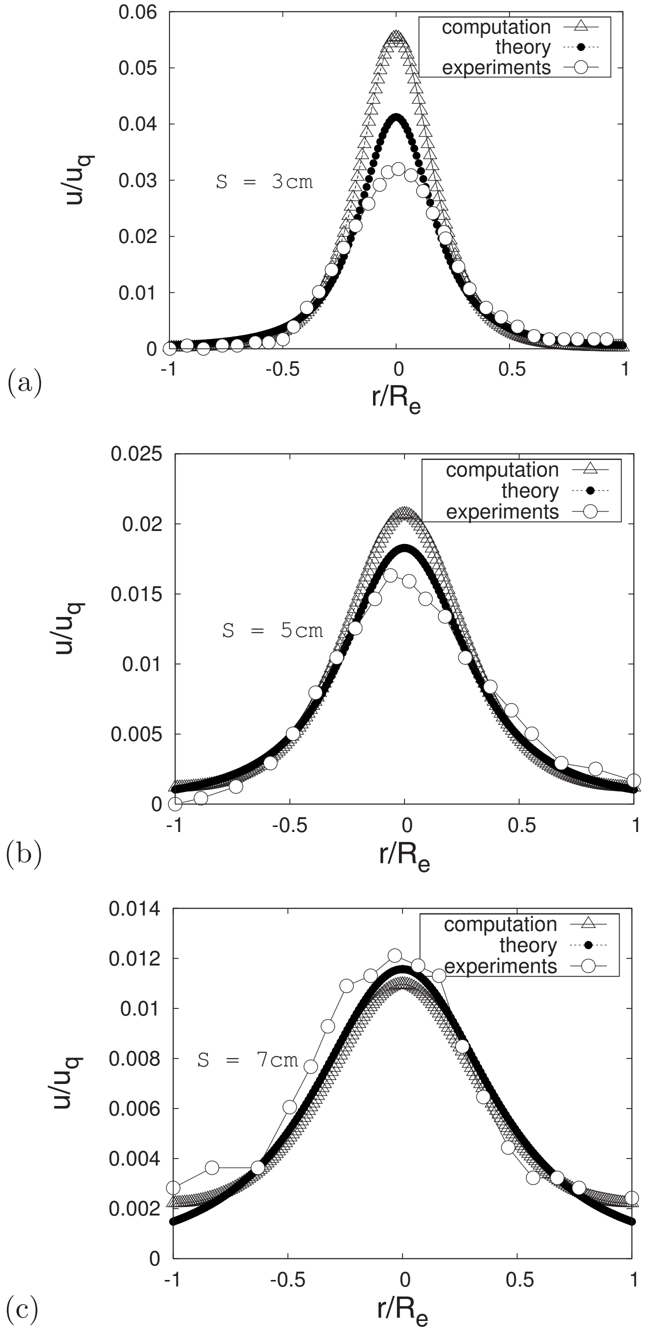

FIG. 10. Comparison between theoretical, experimental, and numerical results for the dimensionless vertical velocity. The reference velocity value is the average injection velocity $u_q \approx 6.3$ cm/s. Different S values are tested: (a) 3 cm, (b) 5 cm, and (c) 7 cm. The experiments are carried out with the bed made of glass beads and at a flow rate of 40 l/h. $d_i = 15$ mm.

manually evaluated for each image. The distance traveled by the dye between two images taken at different times is calculated and the associated velocity determined.

Figure 10 shows examples of comparison between theoretical, experimental and numerical results for the velocity u. The values of u are normalized by the average injection velocity $u_q = 4Q/\pi d_i^2$. For $S = 3$ cm [Fig. 10(a)], differences are observed between theoretical, computational and experimental results near the axis of symmetry. This shows that the effect of the injection is still strong for tested bed thickness. However, the differences decrease progressively with increasing S until $S = 7$ cm [Figs. 10(b) and 10(c)]. This shows that the aspect ratio d_i/S needs to be smaller than 0.2 in order to assimilate an extended source to a punctual one.

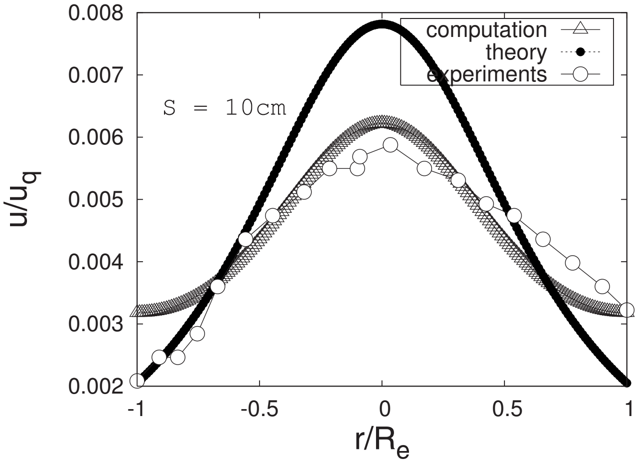

FIG. 11. Comparison between theoretical, experimental, and numerical results for the dimensionless vertical velocity. The experiments are carried out with the bed made of glass beads and at a flow rate of 40 l/h. Experimental parameters are $d_i = 15$ mm and $S = 10$ cm. The computation agrees with the experiments whereas the point source theory is no longer applicable. This figure underlines the effect of the confinement in the experiments for high values of S ($S/R_e \sim 1$).

From Fig. 10 it appears that the experiments coincide better with theory than computations. This probably shows that the real injection is not a jet but something much more similar to a source. It is then very likely that the injection is surrounded by a fluidized area bordered by an arch of grains. In that case, the liquid probably diffuses isotropically through a "spherical wall" as if it were emitted by a source. Above a certain threshold of flow rate, this cavity begins to grow and move upwards by destruction of the arch [regime (ii)] and finally opens up the chimney.

Figure 11 shows the case of $S/R_e = 0.833$ where the effect of the confinement becomes very high. In this figure the experimental data are observed to be in better agreement with computations. This is not surprising since the point source model cannot be valid in such a situation. Furthermore, for large S/R_e ratio any comparison with experiments becomes extremely difficult as the flow velocities at the bed surface are small and therefore the experimental error becomes of the order of the measurement itself.

The above comparisons validate the hypothesis of Darcy's flow in regime (i) and show that aspect ratios $S/R_e \approx 0.6$ and $d_i/S \lesssim 0.2$ are needed in order to have a good representation of a punctual source in an infinite domain by a limited box.

It is interesting to notice in regime (i) the existence of a coupling between the filtration flow exiting the granular bed (at the bed surface) and the flow in the water layer. The filtration flow induces locally and by viscosity, an upward flow from the surface of the bed towards the air-water interface. As the filtration flow has largest velocities near the axis

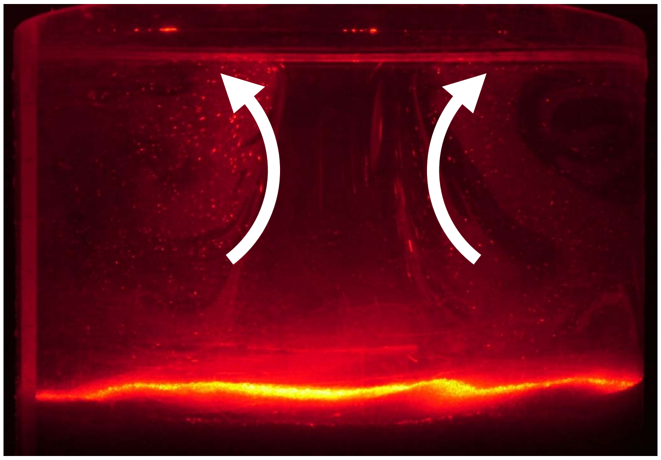

FIG. 12. (Color online) Visualization of the meridian plane of the water layer. This visualization is enabled using a laser sheet along the diagonal axis of the cylinder. The laser lightens small clay particles (dirts) in suspension in the tank's water. The arrows indicate the sense of rotation. The central high speed core coming from the porous medium appears clear of markers (dirt) which were present initially in the water layer but not in the injected flow. Glass beads were used in the experiment. The flow rate was set to 45 l/h and for a bed thickness of $S=3$ cm and an a jet size of $d_i=15$ mm.

of symmetry, a converging flow coming from infinity towards the symmetry axis arises near the bed surface (the symmetry axis acting like a two dimensional sink). On the other hand, near the air-water interface the liquid is sent back toward the periphery (diverging flow) and the symmetry axis acts like a two dimensional source. The fluid motion in the water layer is shown in Fig. 12. We have estimated the horizontal velocities at the air-water interface knowing the flow rate and the water evacuation section when the water pours out of the tank over the cylinder wall. The order of magnitude of horizontal velocities were found to be around 1 mm/s which validates the Dirichlet condition $\hat{p}=0$ used at the bed surface in our theoretical and numerical models.

Despite the simplicity of the theoretical model and the visualization techniques, present experiments are sufficient to confirm the interpretation of this regime as a flow in a porous medium. It is therefore possible to simplify the associated dimensional analysis. For the flow in the porous medium, the set of physical parameters involved in the equations is reduced to K_D in the equation for u and none for the equation for $\hat{p}$. The boundary conditions are limited to the initial pressure at the surface of the bed $\hat{p}=0$ at $z=-W$ and to the injection characterized by a pressure $\hat{p}_i$ and d_i at $z=-(S+W)$. By assuming that the radial extension of the experimental setup is large enough to be assimilated to infinity, the local driving pressure, $\hat{p}$, in a steady state is then a function of $\{\hat{p}_i, S, d_i, x_k\}$, where $x_{k=1,2,3}$ represents symbolically the local coordinates. Here, the water layer thickness W does not appear in the set because of the invariance by translation of the space origin. The dimensionless form of the driving pressure can be written as

$$\hat{p} = \hat{p}_i p^*\left(\frac{S}{d_i}, \frac{x_k}{d_i}\right), \tag{2}$$

where p^* is a dimensionless function. We now express the Darcy law as a function of the dimensionless pressure gradient G^*:

$$\vec{U} = -\frac{K_D \hat{p}_i}{d_i} G^*\left(\frac{S}{d_i}, \frac{x_k}{d_i}\right). \tag{3}$$

A spatial integration of Eq. (3) gives

$$Q = K_D \hat{p}_i d_i Q^*\left(\frac{S}{d_i}\right) \text{ or } \hat{p}_i = \frac{Q}{K_D d_i} P^*\left(\frac{S}{d_i}\right), \tag{4}$$

where Q^* and P^* are dimensionless functions. This means that since d_i/S is given, $\hat{p}_i$ and $Q/K_D d_i$ are equivalent in the set of parameters.

Note that, in the case $S\to\infty$ the solution becomes asymptotically a point source and identification for $R_s \gg d_i$ yields: $\hat{p}_i=Q/2\pi K_D d_i$, $Q^*=1/P^*=2\pi$, and $G^*\to -d_i^2/R_s^2$. However, in this case, $\hat{p}_i$ may no longer be interpreted as an injection pressure. Nevertheless, it is interesting to give a universal interpretation of $\hat{p}_i$. By calling $\vec{U}_1$ the velocity at $R/d_i=1$ on the symmetry axis, one finds that for $S\to\infty$ this velocity is linked to $\hat{p}_i$ by $\vec{U}_1=-(K_D\hat{p}_i/d_i)G^*[\infty,(R/d_i)=1]$ with $G^*[\infty,R/d_i=1]\sim -1$. Therefore, $\hat{p}_i/d_i$ becomes the order of magnitude of the pressure gradient at a distance of the order d_i from the injection center.

B. Regime (iii): Fluidization regime

This regime is characterized by a quasicylindrical vertical chimney inside which the grains are in motion. The diameter of the chimney is almost independent of the size of the injection for a given flow rate. For each given height S, the regime takes place above a reproductible flow rate $Q=Q_f$ but disappears for a value $Q=Q_d$ lower than Q_f. These behaviors are explained here thanks to few experimental data and a simple physical model. In the model, the chimney is considered as a cylinder of basis Σ function of Q only.

At $Q=Q_d$, the vertical hydrodynamical forces compensate the effective weight of the grains in the chimney. Therefore, when Q decreases to Q_d, the equilibrium can be written with variation $\Delta\hat{p}$ of the driving pressure between $z=-S$ and $z=0$. Here, the z origin is taken at the bed surface where $\hat{p}=0$. This equation is

$$\alpha \rho_a S \Sigma_d g = \Delta\hat{p}\Sigma_d, \tag{5}$$

where α is the volume fraction of the grains, Σ_d is the base area of the chimney for $Q=Q_d$ and $\rho_a=\rho_G-\rho$ is the density difference between the grains (ρ_G) and the fluid (ρ). Since for $Q=Q_d$ the grains reach their maximum compaction, α can be considered as constant in the whole chimney. By neglecting the viscous friction on the lateral boundary of the chimney, the equilibrium can be written identically for each slice dz of the chimney:

$$\alpha\rho_a g = -\frac{d\hat{p}}{dz}. \tag{6}$$

At this level of compaction the chimney can also be considered as a cylinder of solid porous medium with a one dimensional flow inside. Therefore, the associate flow rate, Q_{vd} can be expressed as

$$Q_{vd} = -K_D\Sigma_d\frac{d\hat{p}}{dz} = K_D\alpha\rho_a g\Sigma_d, \tag{7}$$

with the driving pressure at $z=-S$ being $\widehat{p_{-S}}=\alpha\rho_a gS$. Note that a similar expression can be obtained using the Richardson-Zaki expression [30] which leads to

$$\frac{d\hat{p}}{dz} = \frac{\alpha\rho_a g}{v_S(1-\alpha)^n\Sigma_d}Q_{vd}, \tag{8}$$

where $v_S=\rho_a g d^2/18\mu$ is the Stokes velocity of a single particle of diameter d falling in a liquid of dynamic viscosity μ, and n is approximately equal to 4.5 [19]. Both expressions of dp/dz are equivalent if $K_D=v_S(1-\alpha)^n/\alpha\rho_a g$. Taking the Stokes approximation yields

$$K_D = \frac{(1-\alpha)^n d^2}{18\alpha\mu}. \tag{9}$$

This expression is one version of the well known Kozeny-Carman formulas for permeability of a porous medium. The exponents of α and $(1-\alpha)$ are not exactly those generally used (respectively 2 and 3) but these coefficients are extremely empirical and controversial [31]. This is irrelevant for our purpose, since K_D can always be adjusted to fit experiments.

The important fact here is that when Q decreases to Q_d the chimney behaves as a one dimensional porous medium in which the pressure varies linearly. Nevertheless, present phenomenon differs from the classical fluidization because the lateral wall of the tube is also porous. Therefore, the injection is still a source of fluid for the surrounding medium. For sufficiently large S/d_i and R_e/S values, the model of Sec. IV A still holds. The pressure induced by this source in the surrounding medium is $\hat{p}=Q_p/2\pi K_D\sqrt{r^2+(z+S)^2}$, where Q_p is the flow rate through the nonfluidized porous medium. The value of Q_p is obtained by identifying the pressure in the chimney and the surrounding medium at $z=-S$ and $r=R_\Sigma$, the lateral boundary of the jet. This gives

$$Q_p = 2\pi K_D R_\Sigma\widehat{p_{-S}} = 2\pi R_\Sigma K_D\alpha\rho_a gS. \tag{10}$$

Finally the total flow rate Q_d is

$$Q_d = K_D\alpha\rho_a g\Sigma_d\left(\frac{2\pi R_\Sigma S}{\Sigma_d}+1\right). \tag{11}$$

According to this formula, the linear dependency of Q_d with respect to S is due to the additional flow inside the nonfluidized porous medium surrounding the chimney. The ratio between this flow rate Q_p and Q_{vd} is simply the ratio of the lateral surface of the jet and its section.

For Q_f it is necessary to take into account the solid friction at the lateral boundary of the chimney. Just at fluidization, pressure $\widehat{p_{-S}}$ must counterbalance the weight of the particles and the friction. As a first approach, we can suppose that the grains are small and numerous in the chimney. At the highest compaction level, the stress paths are almost isotropic and homogenous. The porous matrix can be considered as a solid. In that case, the linearity of Q_f can be explained by a stick-slip behavior. Since the pressure of the water decreases very rapidly with the distance from the source (Sec. IV A) the granular media is essentially submitted to the bottom pressure which pushes it up. Fluidization takes place when this "solid" begins to move under the effect of this pressure which destroys the gravity-induced cohesion of the medium in the limited box. This happens if

$$\Delta\hat{p}\Sigma_f > \alpha\rho_a gS\Sigma_f + \mu_s\Delta\hat{p}\Sigma_f, \tag{12}$$

where μ_s is the average static friction coefficient of the cylinder before fluidization. This model is similar to that of Ref. [13] in the case of seepage erosion but with the addition of grain frictions for the onset of fluidization. Note that here, friction is considered as proportional to the global pressure force responsible for the displacement. At the equilibrium just before fluidization Eq. (12) gives $\Delta\hat{p}=\alpha\rho_a gS/(1-\mu_s)$. Now using the same reasoning as for Q_d, one obtains for Q_f

$$Q_f = \frac{K_D\alpha\rho_a g\Sigma_f}{1-\mu_s}\left(\frac{2\pi R_\Sigma S}{\Sigma_f}+1\right) \tag{13}$$

and $\widehat{p_{-S}}=\alpha\rho_a gS/(1-\mu_s)$. The measures of μ_s for the present grains were carried out using the method of a very slowly rotating drum (see, e.g., [32]) which was previously fully filled with water and half filled with granules. The measures give $\mu_s\approx 0.64$ and $\mu_s\approx 0.51$ for sand and glass beads, respectively. By substituting these values into Eq. (13) and comparing Eqs. (13) and (11), one finds $Q_f/Q_d\approx 2.8$ and $Q_f/Q_d\approx 2.0$ for sand granules and glass beads, respectively.

For the case of sand granules, the above results show a very good agreement with the experiments where from Fig. 6(a) one finds the ratio $Q_f/Q_d\approx 3$. This means that just at fluidization, the injection pressure is about three times the pressure needed to balance the particles' weight. That explains the explosive start of the fluidization as suddenly, most of the pressure is converted into kinetic energy. Pressure drops at the injection because only the weight of the particles has to be compensated. As a consequence, the flow in the surrounding porous medium decreases as the flow is divided into two very different subflows: (1) The one-dimensional "chimney flow" (2) and the slow Darcy flow.

For the case of glass beads the theoretical results appear to differ slightly from the experiments as from Fig. 6(b) one finds $Q_f/Q_d\approx 1.24$. It follows that the model of elastic solid does not hold for the glass beads. Indeed, in this case the fluidization drives from a transitional state [regime (ii)] which will be detailed in section IV C. Our model can be interpreted as the incompressible and isotropic limit of the fluidization process. In the case of glass beads, the size and the particular shape of the grains not only reduce the friction coefficient but also the local stability of the arches and stress paths. This induces local instabilities that propagate a fluidization front vertically from the source to the top of the bed.

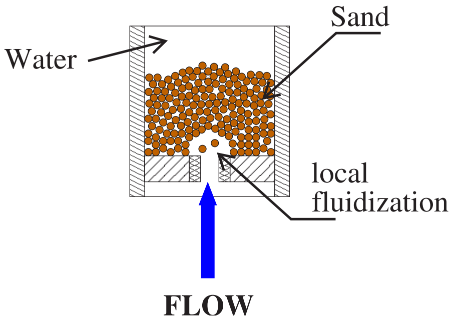

FIG. 13. (Color online) A sketch of the local fluidization around the injection hole.

It must be underlined that neither the theoretical model nor the experiments can be extrapolated toward $S=0$. This is due to the specific properties of a narrow layer of granular material which would show a more hydrodynamical behavior. The study of this behavior is out of the scope of this work and will not be discussed further.

Present theory allows to obtain a relation between section Σ and Q_d or Q_f. Limiting our purpose to the case $R_\Sigma/S \ll 1$ we have

$$\Sigma_d \simeq \sqrt{\frac{Q_d}{\alpha K_D \rho_a g}}$$

or

$$\Sigma_f \simeq \sqrt{\frac{Q_f(1-\mu_s)}{\alpha K_D \rho_a g}}.$$

This shows that Σ depends on the flow rate and on the granular medium properties but not on d_i independently. Nevertheless, an explicit expression for $\Sigma(S,Q,z)$ needs a good description of the solid phase in terms of internal forces and friction thresholds which are not yet available at this state of the art.

C. Regime (ii): A transitional state

The existence of regime (ii) can be explained qualitatively from considerations made in Sec. IV B. This regime is stable if the global displacement of the compacted particles does not immediately destroy the internal cohesion. This regime probably corresponds to the existence of a fluidized area located around the injection where the solid phase could be maintained stable by some arch effects (Fig. 13). Such a situation has commonly been reported in literature in the case, for instance, of a granular bed lying on a tapered surface [3,4,6]. From a physical point of view, this partial and local fluidization decreases the injection pressure by increasing the interface between the porous medium and the injected flow. Therefore, it allows a delay for the global fluidization.

It is interesting to note that the deformation of the bed surface observed during the transitional states, could, possibly, be associated with arch formation near the source.

Arch formation is probably easier for bony sand granules than for spherical glass beads, granting them a higher resistance to pressure near the source. The difficulty for glass beads to form arches could explain the smaller bed deformation. Furthermore, it might explain the difference found between theory and experiments in the case of glass beads (Sec. IV B). Indeed, an internal and local fluidized area at the source might be larger for the spherical granules since their arches can only resist low pressures. Formula for Q_f is therefore only applicable for very dense and "cohesive" materials. One way of giving some mathematical unification to this phenomenon is to consider the propagation of a front of fluidization in a cohesive material. From the point of view of the mass conservation of the grains, the one-dimensional local equation is

$$\frac{\partial \phi}{\partial t} + \frac{\partial \phi v}{\partial z} = 0,$$

where ϕ is the local grain volume fraction and v their vertical velocity. Instead of papers [33–35] where a continuous fluidized bed was studied, here the issue is the case of a discontinuity between a fluidized and a nonfluidized state. The continuous equation has to be replaced by the equivalent Hugoniot equation:

$$[\phi]\omega = [\phi v],$$

where ω is the discontinuity velocity along the vertical axis and the brackets mean a difference between the upstream and downstream faces of the discontinuity. This gives

$$\omega = \frac{\phi_d v_d}{\alpha - \phi_d},$$

where v_d is the modulus of the downstream velocity, α the static medium solid volume fraction and ϕ_d the downstream particle volume fraction. In the case of an "incompressible" medium $\alpha \approx \phi_d$, and ω becomes very high. The chimney is fluidized instantaneously and the above model of "solid extrusion" holds. On the contrary, in the case of an expanding cavity, the beads velocity is zero upstream and equal to the Stokes velocity v_s downstream since ϕ_d is small in the cavity. Therefore, the front velocity is given by

$$\omega \approx \frac{\phi_d v_s}{\alpha}.$$

In such a case, regime (ii) is expected to have a long duration. In this case, the analysis of papers [33–35] becomes more relevant than the previous extrusion model since the fluidization front propagates with a velocity comparable to the particles. These authors underlined the effect of a parameter Ω, derived as a combination of a Reynolds and a Froude numbers of the solid phase, on the "bubbling" nature of the fluidized bed. Here, this parameter could control the stability of the cylindrical chimney. Nevertheless, in the case of a fluidization front, the cohesive nature of the solid matrix and the arches is essential. It gives rise probably to a kind of surface energy that is not taken into account in the equations used in Refs. [33–35]. That is why present analysis is based only on the mass conservation equation and heuristic considerations.

Of course, all of this holds if some reasonable ratio is assumed between the size of the chimney and the particle diameter. Duru *et al.* [20] emphasized the role of the bed to particle diameter ratio R which has to remain larger than 10 in order to avoid particle jamming or arching effects within a tube of fluidized particles. In the present study where the arching effects seem to be present in the regime (ii), one can speculate on the wall effect on this ratio R. Indeed, in this regime where the bed shows a partial fluidization of the chimney, it is interesting to calculate R in this configuration where the chimneys' walls were found to depend mainly on the particles characteristics. By assuming that the diameter of the bounding wall of the fluidized section of the bed in regime (ii) is roughly of the same size than the chimney in the regime (iii), one finds $R \approx 20/[(0.450+0.250)/2]=57$ for sand granules. This value is substantially larger than 10 above which particle jamming and arch effects are not supposed to take place [20].

V. SUMMARY

The effect of a punctual water jet on a granular bed was investigated experimentally, theoretically and numerically. It was found that three distinct regimes associated with the flow rate Q appear to outline the bed's behavior. For sufficiently small Q the bed remains motionless and acts as a porous medium [regime (i)]. At sufficiently large Q values, a transitional regime takes place and the bed becomes deformed [regime (ii)]. Finally, it "explodes" and a fluidization limited to an area above the jet is observed if Q is increased further [regime (iii)]. This fluidization creates a chimney-like fluidized area in the bed within which the granules are in motion. The results show that the onset for fluidization as well as the size of the chimney appear to be almost independent of the size of the water jet. A difference between the onset of fluidization and defluidization was also observed.

The effect of boundaries on the flow motion inside the motionless bed were investigated theoretically and numerically for the regime (i). The results were compared to experimental data obtained with various thicknesses of the bed. The investigations show that a ratio between the injection diameter and the bed thickness smaller than ≈0.2 is needed to assimilate the water jet as a punctual source. Furthermore, a ratio of 0.6 between the bed's thickness and the cell's radius is found to be necessary for a good representation of a localized source in an infinite domain while limited by a box.

The linear dependence of the onset of fluidization with the height of the bed observed in the experiments has been explained by a point source model and related to the "leaks" through the non fluidized matrix around the chimney. The hysteresis between the onsets was related to the cohesion of the compacted bed by a simple model that shows a very good agreement for bony sand granules. For a less cohesive bed and for the transitional regime (ii) some directions of research are indicated on the basis of the relevant literature.

ACKNOWLEDGMENTS

The authors would like to thank undergraduate students N. Champavert and S. Leroy who carried out some of the experiments presented here.

[1] M. J. Rhodes, *Introduction to particle technology* (John Wiley & Sons, Chichester, England, 1998).

[2] C. Vogt, R. Schreiber, G. Brunner, and J. Werther, Powder Technol. **158**, 102 (2005).

[3] Y. Peng and L. T. Fan, Chem. Eng. Sci. **52**, 2277 (1997).

[4] S.-Y. Son, D. Hyun Lee, G. Young Han, D. Joon Kim, S. Jun Sim, and S. Done Kim, Korean J. Chem. Eng. **22**, 315 (2005).

[5] S. L. Soo, *Fluid Dynamics of Multiphase Systems* (Blaisdell Publishing Company, Waltham, MA, 1967).

[6] Y. Peng and L. T. Fan, Chem. Eng. Sci. **50**, 2669 (1995).

[7] W. Zhong and M. Zhang, Chem. Eng. Sci. **60**, 315 (2005).

[8] R. Y. Hong, Q. J. Guo, G. H. Luo, J.-Y. Zhang, and J. Ding, Powder Technol. **133**, 216 (2003).

[9] R. N. Weisman and G. P. Lennon, J. Waterway, Port, Coastal, Ocean Eng. **120**, 468 (1994).

[10] R. N. Weisman, G. P. Lennon, and E. W. Roberts, J. Hydraul. Eng. **114**, 502 (1988).

[11] G. P. Lennon and R. N. Weisman, J. Hydraul. Eng. **121**, 838 (1995).

[12] A. W. K. Law, J. Hydraul. Eng. **121**, 653 (1995).

[13] A. E. Lobkovsky, B. Jensen, A. Kudrolli, and D. H. Rothman, J. Geophys. Res., Earth Surface **109**, F04010 (2004).

[14] L. O. Owoputi and W. J. Stolte, Hydrolog. Process. **15**, 13 (2001).

[15] N. Schorghofer, B. Jensen, A. Kudrolli, and D. H. Rothman, J. Fluid Mech. **503**, 357 (2004).

[16] G. M. Homsy, Appl. Sci. Res. **58**, 251 (1998).

[17] E. Guazzelli, in *The Physics of Granular Media*, edited by H. Hinrichsen and DE Wolf (Wiley-VCH, Berlin, 2004).

[18] S. Sundaresan, Annu. Rev. Fluid Mech. **35**, 63 (2003).

[19] R. Jackson, *The Dynamics of Fluidized Particles*, Cambridge Monographs on Mechanics (Cambridge University Press, Cambridge, UK, 2000).

[20] P. Duru, M. Nicolas, J. Hinch, and E. Guazzelli, J. Fluid Mech. **452**, 371 (2002).

[21] J. Jung and D. Gidaspow, J. Nanopart. Res. **4**, 483 (2002).

[22] N. G. Deen, W. Dijkhuizen, G. A. Bokkers, M. van Sint Annaland, and J. A. M. Kuipers (unpublished).

[23] A. Khalili and M. Stöhr, Phys. Rev. E **73**, 036301–1 (2006).

[24] J.-C. Géminard (private communication).

[25] L. Gostiaux, H. Gayvallet, and J.-C. Géminard, Granular Matter **4**, 39 (2002).

[26] P. G. Cizmas, A. Palacios, T. O'Brien, and M. Syamlal, Chem. Eng. Sci. **58**, 4417 (2003).

[27] R. Ojha, N. Menon, and D. J. Durian, Phys. Rev. E **62**, 4442 (2000).

[28] J. R. L. Allen, Developments in sedimentology **30B**, 293 (1982).

[29] L. H. Chen and J. R. Too, *Encyclopedia of Fluid Mechanics* (Gulf Publishing Company, Houston, TX, 1986), Vol. 4, pp.

1161–1184.
[30] F. J. Richardson and W. N. Zaki, Trans. Inst. Chem. Eng. **32**, 35 (1954).
[31] M. Palassini and A. Remuzzi, Am. J. Physiol. Renal Physiol. **274–1**, 223 (1998).
[32] J. Duran, *Sables, poudres et grains* (Eyrolles Sciences, Paris, 1997).
[33] K. Anderson, S. Sundaresan, and R. Jackson, J. Fluid Mech. **303**, 327 (1995).
[34] B. J. Glasser, I. G. Kevrekidis, and S. Sundaresan, J. Fluid Mech. **306**, 183 (1996).
[35] B. J. Glasser, I. G. Kevrekidis, and S. Sundaresan, J. Fluid Mech. **334**, 157 (1997).